A black hole particle swarm optimization method for the source parameters inversion: application to the 2015 Calbuco eruption, Chile

Leyang Wang [a], Xibo Jin [a,b], Wenbin Xu [c,d,*], Guangyu Xu [a]

[a] *Faculty of Geomatics, East China University of Technology, Nanchang, 330013, China*
[b] *School of Geodesy and Geomatics, Wuhan University, Wuhan, 430072, China*
[c] *School of Geosciences and Info-Physics, Central South University, 410083, Changsha, China*
[d] *Key Laboratory of Metallogenic Prediction of Nonferrous Metals and Geological Environment Monitoring (Central South University), Ministry of Education, Changsha, 410083, China*

ARTICLE INFO

ABSTRACT

The traditional genetic algorithm and simulated annealing methods have been widely used in geophysical modeling. However, these nonlinear inversion methods require a lot of calculations, many control parameters and are unstable. In this paper, a particle swarm optimization algorithm combined with black hole strategy (BH-PSO) is proposed to solve these problems. The comprehensive experiments show that the BH-PSO method consumes less time than the simulated annealing (SA) method and has a higher accuracy than the genetic algorithm (GA). It is more applicable to the inversion of parameters of volcanic magma chamber, and easier to be generalized to other kinematic source parameters inversion. Based on BH-PSO method, Sentinel-1 data, composite dislocation model (CDM), Yang model and Mogi model, the magma chamber parameters of Calbuco eruption in 2015 were retrieved. The results show that the RMSE of CDM model is 1.1 cm, which can better fit the surface deformation than the Mogi model and Yang model. The final results show that the magma chamber is located about 0.8 km northeast of the crater, about 9 km below the surface, and the total volume of the erupted volcanic material obtained with the CDM Model is of 0.209 km^3, without considering dense rock equivalent.

1. Introduction

The Calbuco volcano (Fig. 1) is one of the most dangerous Chilean volcanoes (Lara et al., 2011). This volcano is located in the Andes Mountains, southern Chile, at the coordinates 41°19′48″ S, 72°37′06″ W, with an elevation of 2003 m. (Stern, 2004; Siebert et al., 2011). This volcanic area is active, with more than 12 volcanic eruptions in history. The largest eruption occurred between 1893 and 1895, and two smaller eruptions occurred in 1961 and 1972 (Selles et al., 2011). After 43-years of silence, this volcano produced a new round of eruptions beginning on April 22, 2015 without any warning. These eruptions greatly affected the local environment and the personal safety and property of the residents. At the same time, the volcanic ash and harmful gases emitted during the eruption also spread globally as a result of atmospheric activities. Studies have shown that both Africa and Antarctica were affected by the harmful gases emitted by the eruption (Sangeetha et al., 2018; Stone et al., 2017; Zhu et al., 2018; Ivy et al., 2017). Therefore, this eruption of the Calbuco volcano had a substantial impact not only on local areas, but also on the global air quality. It is of great practical significance to study the Calbuco volcano and explain its eruption mechanism.

After the eruption of the Calbuco volcano in April 2015, a number of researchers and research institutes conducted a multifaceted study on this volcano. Among them, Matoza et al. (2018) determined the location of the earthquake source associated with the volcanic activity. Liu et al. (2017) studied the effects of this volcanic activity on the atmospheric ionosphere. Romero et al. (2016) studied the state of volcanic ash deposits. Ebmeier (2016) studied the effects of this volcanic eruption on the regional surface deformation. Eaton et al. (2016), Romero et al. (2016); Pardini et al. (2018), and Castruccio et al. (2016) analyzed the volume of volcanic material eruptions. Arzilli et al. (2019) estimated the pre-eruptive pressures, temperatures and depths of the Calbuco 2015 eruption using petrological data, and investigated the triggering mechanism of the eruption. Morgado et al. (2019) estimated the location of the magma chamber between 5.5 and 9.5 km depth using petrological data. Namur et al. (2020) agree with Arzilli et al. (2019) in terms of the

---

triggering mechanism and the location of the main magma chamber which is located between 8 and 11 km depth. Namur et al. (2020), on the basis of petrological data, invoked a migration of the magma into a subsurface storage region a few weeks to months before the eruption. Delgado et al. (2017) inverted the pressure source parameters of this volcanic event; this was achieved by using the single-source Mogi model. Delgado et al. (2017) also noted that the quality of their data may be problematic, and the shapes of the magma chamber of the InSAR data may be disturbed, so the inversion results may be biased. The results obtained by the single source model inversion of the pressure source do not effectively explain the surface observation variables in the far field (Delgado et al., 2017). Rather, their single source model inversion of the pressure source mainly estimates the deformation near the crater; unfortunately, volcanic ash affects the observations, causing the estimates to deviate from the actual values.

Many inversion methods are available, including the genetic algorithm (GA) and its improved algorithms (Tiampo et al., 2000; Nunnari et al., 2005; Gambino and Guglielmino, 2008) and the improved simulated annealing (SA) algorithm (Shirzaei and Walter, 2009). However, the SA and GA have many design control parameters. They also suffer from a low computational inversion efficiency, and are difficult to obtain the global optimal value quickly and effectively in practical applications (Shi and Wang, 2008). The particle swarm optimization (PSO) (Eberhard and Kennedy, 1995) algorithm is a fast and effective geophysical inversion method, which does not dependent on the initial model and can search for the global extrema. The PSO has been widely used in many fields, such as mechanical design (He et al., 2004), shop scheduling (Sha and Hsu, 2008), complex network clustering (Gong et al., 2014), image segmentation (Ghamisi et al., 2014), and inversion of fault parameters (Feng and Li, 2010; Wang et al., 2017), due to its small number of control parameters and strong search capabilities. However, the PSO algorithm needs to be improved when overcoming

local minima during the inversion search process. The black hole elimination strategy (Hatamlou, 2013) can help solve the problem of local optimality and global optimization. Here, we propose a BH-PSO algorithm to invert for volcanic magma chamber parameters that considers both the advantages of both methods for the inversion of source parameters. We apply the BH-PSO method to invert for volcanic magma chamber parameters of Calbuco.

To date, the most commonly used model in volcano research is the Mogi model, which can be traced back to 1958. In that year, Japanese scholar Kiyoo Mogi proposed a pioneering model based on the Yamakawa theory (Mogi, 1958). This model relates the magma pressure source parameters to the volcanic surface deformation using a specific functional relationship (Mogi, 1958). Because the model formula is simple and easy to calculate and has broad applicability, it has been widely used since its introduction, for example, for the Tianchi volcano in China (Chen et al., 2008; Wang and Yu, 2018), Russia's Karymsky volcano (Ji et al., 2018), Mount Sinabung in Indonesia (Hotta et al., 2017) and the volcanoes in the Alaska region, (Wang et al., 2018c). The compound dislocation model (CDM) was proposed by Nikkhoo et al. in 2017 for the inversion of volcanic pressure source parameters (Nikkhoo et al., 2017). Compared with the Mogi model, the advantage of this model is that the shape of the model is not unique. A spherical shape, an ellipsoidal shape and an irregular spatial shape can be obtained through adjusting the parameters, and thus, the shape can be more universal, i.e., closer to the real conditions of underground magma chambers. At the same time, the Mogi model can also be considered as a special existence of the CDM. (Nikkhoo et al., 2017).

The structure of this paper is organized as follows. First, the advantages and disadvantages of the BH-PSO algorithm are analyzed. Then, the radius selection strategy of the black hole algorithm is combined with the PSO algorithm to obtain the BH-PSO algorithm. And the BH-PSO algorithm is applied to the inversion of the Mogi model, Yang
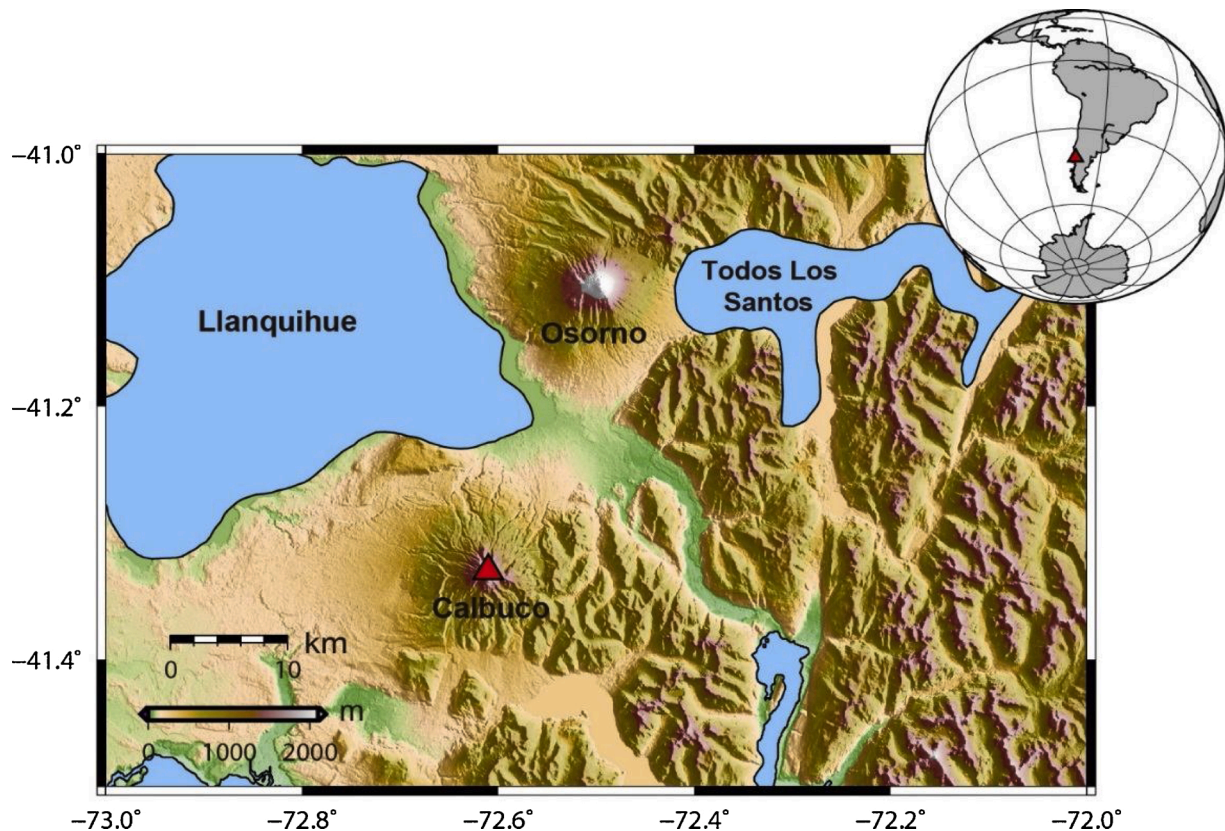
Fig. 1. The topographic structure of the study area.
Red triangle represents the top of the Calbuco volcano.

model and CDM. Through a simulation experiment, the applicability of the proposed method to the volcano Mogi model, Yang model and CDM is verified, and compared with the applicability of both the GA and the SA algorithm commonly used at this stage. Finally, the Calbuco volcano is studied by the Mogi model, Yang model and the CDM, by comparing the inversion results with different observation data. A more suitable inversion model is determined, and pressure source (magma chamber) parameters are obtained with a superior accuracy.

2. Black hole particle swarm optimization method

2.1. Black hole algorithm

The black hole algorithm (Hatamlou, 2013), is an algorithm for solving cluster analysis problems. The idea of the algorithm as follows: to find the optimal solution for the objective function, the various parameter sets involved in the calculation of the objective function are used as the planet (for example, the volcanic magma pressure source parameters $(x_0 , y_0 , D , \Delta V)$ in the Mogi model), and the initial calculation is performed by referring to the attraction and phagocytosis of the black hole to the planet. First, randomly, one of parameters (m_i) in the initialization is used as a black hole (m_{BH}), all values are attracted by the black hole and move towards the black hole. If some particles appear within the absorption radius of the black hole, these particles will be absorbed by the black hole; and that particles, outside the absorption radius of the black hole, are not absorbed. If a new solution (m_{i+1} corresponding to the f_{BH}) occurs during the operation, the new adaptive solution is treated as a new black hole (m_{BH}), and all particles (except the black hole) are moved to the updated black hole. The black hole continually engulf particles and updates itself (Hatamlou, 2013) until the maximum number of iterations is reached or all particles are absorbed by the black hole, and the black hole parameters $(m_i(t + 1)$ corresponding to $(x_0 , y_0 , D , \Delta V))$ that are finally output under the cutoff condition are the optimal solution parameters. The main calculation formula of the algorithm are as follows:

$$m_i(t + 1) = m_i(t) + r \times (m_{BH} - m_i(t)) \tag{1}$$

$$R = \frac{f_{BH}}{\sum_{i=1}^{N} f_i} \tag{2}$$

where $m_i(t)$ and $m_i(t + 1)$ are the positions of the i th star at iterations t and $t + 1$, respectively, m_{BH} is the position of the black hole, r is a random number in the domain [0, 1], R is the radius of the black hole (the radius here is used to adjust the size of the black hole search space, radius can be used to adjust the search step size(ω), when applied to the particle swarm algorithm), f_{BH} is the target fitness value of the black hole, obtained by the fitness function (in this paper, it is obtained by Eq. (3)), f_i is the fitness value of the i th star, and N is the total number of stars.

2.2. Inversion of the BH-PSO algorithm based on the CDM

The PSO algorithm (Fig. 2) has been verified as fast and effective in geophysical inversion problems (Shi et al., 2009). However, the PSO algorithm easily falls into the local minima during the optimization process, which leads to deviations from the global optimum. In response to this problem, Zhang et al. combined a particle swarm optimization algorithm with a random black hole strategy (Zhang et al., 2008). This combined algorithm speeds up the convergence; however, it is also quick to cause premature convergence and premature loss of the diversity of the solution.

This paper finds that the method of improving in the algorithm problem of Zhang et al. (2008) is mainly to perform a random black hole search under globally optimal conditions. The black hole position is set
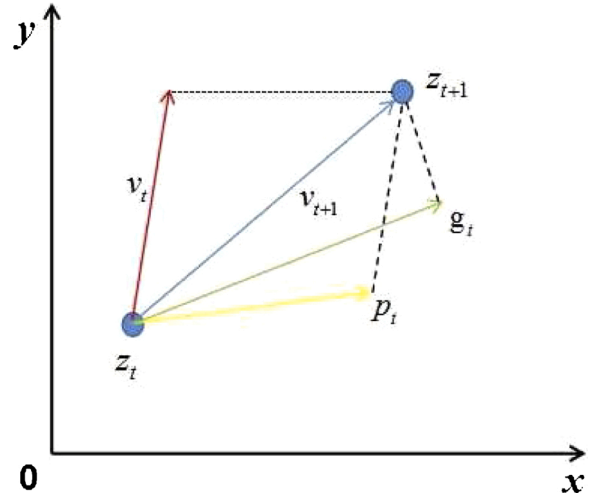

Fig. 2. Iterative diagram of particle swarm algorithm.

by using random numbers, and the extreme value is determined within the radius of the random black hole. However, this method has the following defects:1, The global search cannot be performed well. 2, There is almost no relationship between the magnitude of the random number and the current number of iterations, and the generated black hole cannot solve the relationship between the global optimum and local optima. 3, Because the black hole is random, there is no guarantee that a quick search will be performed at the early stage of the search process, slow searches at the middle and late stages.

To solve the above problems, this paper combines the radius selection strategy of black hole algorithm (Hatamlou, 2013) with the weight of the particle velocity adjustment in the PSO algorithm (Shi and Eberhart, 1998). In addition, m_{BH} in the black hole algorithm is considered to be the global optimal value (f_{gbest}) of the PSO, while $m_i(t)$ is regarded as the local optimal value (f_{pbest}), and the speed of the search is controlled by the ratio of the f_{gbest} and the f_{pbest} (the radius in the black hole algorithm). When using BH-PSO algorithm to search parameters, the search process is controlled by gradually adjusting the weight of search speed. When the ratio (represented by the $\frac{f_{gbest}}{f_{pbest}}$) is large (indicating that the quality of the current global optimal result is poor), the speed weight becomes larger, and the search range is increased to find a better global solution. When the ratio is small (indicating that the current global optimal result is good), there is no need to perform a large-scale search at this time, and the search range is reduced; If the ratio exceeds the known optimal weight [0.4, 0.9], the weight is artificially adjusted to ensure that it is within the optimal range ([0.4, 0.9]). Afterward, the above strategy is adjusted to ensure that the global optimal solution can be obtained at the end of the iteration.

When the BH-PSO algorithm is combined with the CDM or Mogi model for an inversion of volcanic pressure source, the algorithm can be rewritten as follows

$$z_{ij(t+1)} = z_{ij(t)} + \omega \times v_{ij(t)} + c_1 \times r_1 \times (f_{pbest(t)} - z_{ij(t)}) + c_2 \times r_2 \times (f_{gbest(t)} - z_{ij(t)}) \tag{3}$$

where, $Z_{ij(t+1)}$ and $Z_{ij(t)}$ represent the results for the $t + 1$ th and t th iterations respectively (where, Z represent the volcanic source parameter to be sought in the CDM: $x_0, y_0, D, \varphi_a, \varphi_b, \varphi_c, a, b, c$; or the volcanic source parameters to be sought in the Mogi model namely, $x_0, y_0, D, \Delta V$), i is the i th particle, j is the j th parameter, ω is the velocity weight, v is the particle motion velocity, $c_1 t$ and $c_2 t$ are the acceleration factors (the specific values are determined by Eqs. (10) and (11), respectively), r_1 and r_2 are random numbers within [0, 1], $f_{pbest(t)}$ is the individual optimal value of the t th iteration, and $f_{gbest(t)}$ is the global optimal value

of the t th iteration (determined by Eq (3)). The speed weight and acceleration factor are selected as follows:

$$\omega = \begin{cases} \dfrac{f_{gbest}}{f_{pbest}} & 0.4 \leq \dfrac{f_{gbest}}{f_{pbest}} \leq 0.9 \\[3mm] 0.9 - 0.5 \times \dfrac{t}{M} & 0.4 > \dfrac{f_{gbest}}{f_{pbest}}, \dfrac{f_{gbest}}{f_{pbest}} > 0.9 \end{cases} \tag{4}$$

$$c_{1t} = (c_{1s} - c_{1e}) \times \frac{t}{M} + c_{1e} \tag{5}$$

$$c_{2t} = (c_{2s} - c_{2e}) \times \frac{t}{M} + c_{2e} \tag{6}$$

where, M is the maximum number of iterations, $c_{1s} = c_{2e} = 1$, $c_{1e} = c_{2s} = 2.05$. $c_1 t$ and $c_2 t$ change with the number of iterations t. Eq. (4) is the ratio of the fitness of the global optimal value to the individual optimal value as the criterion for adjusting the particle; thus, the speed weight ω changes due to changes in the individual optimal value and the global optimal value. At the same time, a change interval is set to ensure that the change in the speed weight is within the known optimal change interval [0.4, 0.9]. Eqs. (5) and (6) use the acceleration factor control idea of Ratnaweera et al. (2004). When $f_{pbest(t)}$ is greater than $f_{gbest(t)}$, their positions are exchanged to ensure that the final result is globally optimal, and the final output Z is the optimal solution of the volcanic pressure source.

3. Volcanic source models: Mogi, Yang and CDM

3.1. Mogi model

Mogi (1958) pointed out that when the radius of the magma pressure source is much smaller than the source depth, the magma pressure source is placed in an elastic half space, and the crust is considered as a homogeneous elastic medium, the activity of the volcanic magma can be regarded as an equivalent spherical source (Mogi, 1958). Under this condition, the volcanic magma pressure source parameters (x_0, y_0, D, ΔV) and the surface shape variables can be related by a specific functional relationship (the Mogi model is shown in Fig. 3(a)):

$$(U_x, U_y, U_h) = M_{mogi}(x_0, y_o, D, \Delta V, \mu, K) \tag{7}$$

where, U_x is the displacement (deformation) in the x direction, U_y is the displacement (deformation) in the y direction, U_h is the vertical displacement (deformation), (x_0, y_0) are the projection coordinates of the pressure source in the ground plane, D is the depth of the source, ΔV is the magma volume increment, μ is the shear modulus, K is the bulk modulus of elasticity(usually considered $K = \frac{5}{3}\mu$), and M_{mogi} represents the Mogi model.

When using InSAR observations, the following relationship exists between the observed deformation and the deformation simulated by the Mogi model.

$$D_{los} = U_h \times \partial(\alpha) + U_x \times \partial(\beta) + U_y \times \partial(\delta) \tag{8}$$

where, D_{los} denotes the InSAR data, $\partial(\alpha)$ is the conversion coefficient between the surface vertical deformation and InSAR observed deformation, $\partial(\beta)$ is the conversion coefficient between the x direction horizontal deformation and InSAR observed deformation, $\partial(\delta)$ is the conversion coefficient between the y direction horizontal deformation and InSAR observed deformation.

In the inversion of volcanic pressure source parameters based on the Mogi model, the most commonly used evaluation criterion is the fitness function of the best fit between the model analog values and the observed values:

$$f = \sqrt{\frac{\|\boldsymbol{D}_{obs} - \boldsymbol{D}_{los}\|^2}{n}} \tag{9}$$

where, n is the number of observations, D_{los} is the observd surface deformation, and D_{obs} is the simulated value under the Mogi model, which is consistent with $Eq.$ (8).

3.2. Yang model

Yang et al. (1988) proposed this model in 1988 for inversion of volcanic pressure source parameters (Yang et al., 1988). This model is based on the model of Mogi, and Fialko et al. (2001) modified this model in 2002 (Fialko et al., 2001). This model can be used to describe an ellipsoidal underground magma chamber. There are eight parameters related to the magma chamber in this model, which can be used to describe the underground magma chamber. However, this model cannot directly invert the eruption volume of the magma chamber and needs to be calculated again. In this paper, the Yang model is used to relate the pressure source parameters to the surface deformation by the following formula (the Yang model is shown in Fig. 3(b)):

$$(U_x, U_y, U_h) = C_{Yang}(x_0, y_0, D, P, a, b, Plunge, Trend) \tag{10}$$

where, U_x, U_y and U_h are the observed shape variables, x_0, y_0 and D are the pressure source parameters; the definitions of which are consistent with those of the parameters in the Mogi model. a, and b represent the lengths of the two rotating axes of the Yang; $Plunge$ and $Trend$ indicate the angles of the rotation of the magma chamber (Fialko et al., 2001). C_{Yang} represent the Yang models used to integrate the surface deformation and magma source parameters. Under the condition where the surface deformation is known, the pressure source parameters can be obtained by inversion through the Yang model.
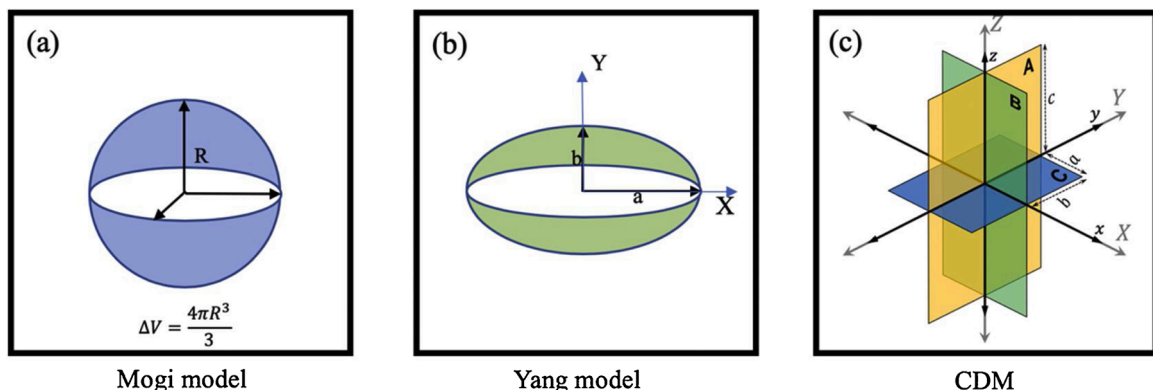

Fig. 3. Schematic diagram of three models.(c) from Nikkhoo et al. (2017).

3.3. Compound dislocation model

Nikkhoo et al. (2017) proposed the CDM in 2017 and applied it to the inversion of volcanic magma chamber parameters. Compared with the Mogi model, the calculation of the CDM is more complicated, and the CDM has no advantage in its inversion efficiency. However, the theoretical basis of the CDM is more complete than that of the Mogi model, and it boasts a more common pressure source. The commonly used Mogi model and the Yang model can be considered as the special cases of the CDM. The CDM can describe pressure sources with a more general shape or irregular shape. Therefore, it is considered that the CDM has an advantage regarding the shape of the pressure source. However, Nikkhoo et al. (2017) also noted that the volume of the magma source obtained by CDM refers only to the volume of new magma that can accommodate intrusion from the outside and does not represent the actual amount of erupted material, whereas the amount of erupted material predicted by the Mogi model refers to the actual eruption volume. Therefore, the amount of erupted magma simulated by the CDM may be less than the actual amount of erupted material. In this paper, the CDM is used to relate the pressure source parameters to the surface deformation by the following formula (the CDM is shown in Fig. 3(c)

$$(U_x, U_y, U_h, \Delta V) = C_{CDM}(x_0, y_0, D, \varphi_a, \varphi_b, \varphi_c, a, b, c) \tag{11}$$

where, U_x, U_y and U_h are the observed shape variables, ΔV, D, x_0 and y_0 are the pressure source parameters; the definitions of which are consistent with those of the parameters in the Mogi model. a, b and c represent the lengths of the three rotating axes of the CDM; the origin of the rotating shaft is located at the center point of the magma chamber, and a spatial rectangular coordinate system is established with the center point of the magma chamber as the origin. φ_a, φ_b and φ_c indicate the angles of the rotation of the magma chamber around the a, b and c, respectively (Nikkhoo et al., 2017). C_{CDM} represent the compound dislocation models used to integrate the surface deformation and magma source parameters. Under the condition where the surface deformation is known, the pressure source parameters can be obtained by inversion through the CDM. Different from the Mogi model, ΔV is not an independent variable in the CDM; instead, ΔV needs to be obtained by the CDM under the condition that the other nine parameters are known.

In Fig. 3, (a) represents the theoretical shape of the Mogi model, and ΔV is usually used to represent the volume of magma during inversion; (b) represents the theoretical shape of Yang model. In inversion, the long axis a and short axis b are usually used to calculate the volume of magma; (c) represents the theoretical shape of CDM (from (Nikkhoo et al., 2017)). In inversion, three coordinate axis lengths a, b and c are usually used to calculate the volume of magma, and the results calculate the specific lengths of a, b and c.

3.4. Inversion process: taking the CDM as an example

1 Utilize the prior information to determine the interval of values (information can be obtained from previous studies) for each parameter ($x_0, y_0, D, \varphi_a, \varphi_b, \varphi_c, a, b, c$) to be sought. (when using the Mogi model, the input consists of only $x_0, y_0, D, \Delta V$).
2 Run the BH-PSO search algorithm to obtain the initial solution space of the parameters (Z) (determine the solution space by means of random generation).
3 Substitute the initial solution into the CDM and perform the calculation (using Eq.(11)) to obtain the theoretical shape variables (D_{los}) and use Eq.(8) to obtain the corresponding InSAR-observed deformation. (when using the Mogi model, Eq.(7) must be used to calculate the isotropic deformation components).
4 Calculate the fitness values (f by using Eq.(9)) between the theoretical deformation variables (D_{los}) obtained by different parameters and the original InSAR-observed deformation variables D_{los}.

5 Select the optimal parameters to be set in the current solution space (the lowest value of f corresponds to $x_0, y_0, D, \varphi_a, \varphi_b, \varphi_c, a, b, c$) and update the solution space of the parameters (randomly selected in the first iteration, for the second use Eq. (3)–(6)).
6 Determine whether the threshold is reached or whether the maximum number (M) of iterations is reached (the selection of the threshold is related to the accuracy requirements of the inversion).
7 If either the threshold or the maximum number of iterations is reached, the optimal parameter is output and the parameter is used as the optimal solution (Z_{ij}). If not, the process returns to step 3.

If the Mogi model or Yang model is used, the search parameters and the external conditions should be reset up, while the BH-PSO algorithm itself is unchanged.The specific process is shown in Fig. 4.

4. Synthetic experiment

4.1. BH-PSO + Mogi

To verify the effectiveness of the inversion method used in this paper, the following simulation experiment was carried out: a volcanic eruption event was simulated on a domain of 20 km × 20 km with the volcanic eruption as the origin at its center. The preset true values of each parameter are shown in Table 1. These parameters are substituted into the Mogi model of a single pressure source for forward modeling. The displacement obtained after the forward modeling is transformed into deformation observation data in the InSAR direction (observation azimuth of ascending orbit is $-10°$, radar wave incidence angle of 23°) and combined with the InSAR data characteristics, to which error following a normal distribution is added (mean of 0, magnitude of 0.5 cm).The values after the error is added, represent the theoretically true observations (Fig. 5).

Fig. 5(a) indicates that that the InSAR-observed deformation values are no errors under the preset true values, (b) indicates that the InSAR-observed deformation values are obtained after adding error of 0.5 cm, (c) is the simulation result using the SA method, (d) is the GA method simulation result (e) is the PSO method simulation result (f) is the BH-PSO method simulation result. (i) is the residual of PSO method inversion. The results are the most obvious, and the residual is mostly $1−2$ cm. The residuals and original observations of (g), (h) and (j) are small. However, there is difference between (g) and (h), especially where the coordinate is (0,0).

As shown in Fig. 5 the pattern after adding the error (d) shows a large deviation from the original pattern (a), and smooth deformation is not formed well; that is, the added error has a great influence on the observation data. Combined with the model characteristics of the simulation experiment, the Mogi model of a single pressure source is employed, and the SA, the GA, the PSO and the BH-PSO, are used to invert for the pressure source parameters. The parameter search interval of the particle swarm algorithm is shown in Table 1, and the simulation results of different methods are recorded in Fig. 5.

The inversion results in Table 1 show that the BH-PSO algorithm can effectively calculate the pressure source parameters when performing the pressure source parameter inversion. The difference between the inversion result and the true value is smaller than the differences in the existing PSO and GA, indicating that the results of the BH-PSO are more accurate than those of these other algorithms. The inversion results of the BH-PSO and the SA are numerically inconsistent, but the difference between the two norms of the two methods reaches the fourth digit after the decimal point, indicating that the accuracy of the BH-PSO is slightly superior. Since the difference between the two norms of the BH-PSO and the SA is very small, this paper considers that these two algorithms are equivalent, the reason why these two methods are equivalent is that the theoretical basis of both of these two methods is to find the optimal solution within the solution space. Although the theoretical basis of the optimization process is different, the iterative method of optimization,
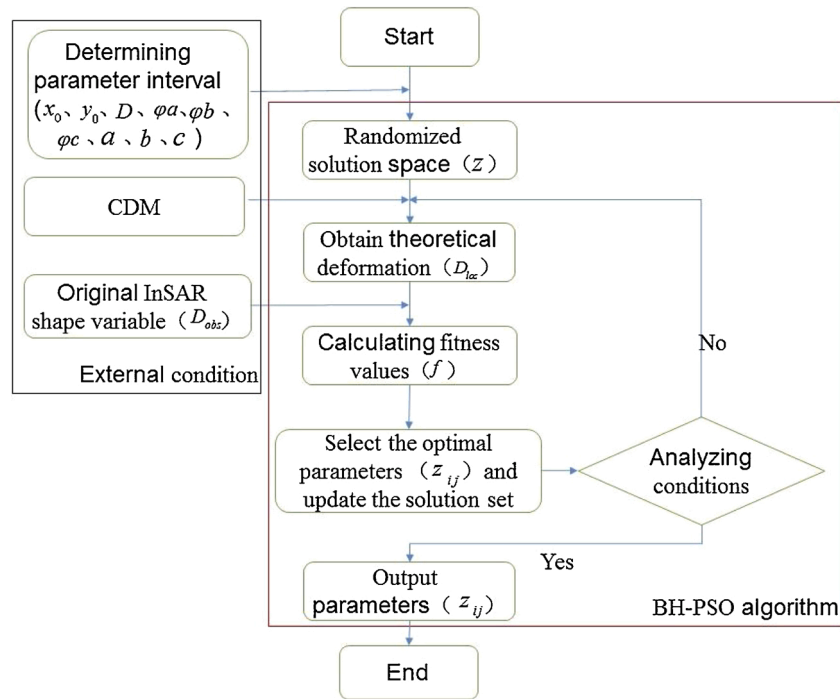
Fig. 4. Flow chart of BH-PSO + CDM inversion.

Table 1
Search intervals of input parameters (Mogi) and inversion results using different methods.

	X/km	Y/km	D/km	$\Delta V/km^3$	time/s	RMSE /cm
Truth	0.00	0.00	5.00	0.01	/	/
SA	−0.07	−0.04	5.05	0.0101	942	0.52
GA	0.13	−0.02	4.95	0.0098	161	0.52
PSO	0.21	0.17	5.10	0.0099	385	0.57
BH-PSO	0.06	−0.02	4.98	0.0099	278	0.50

the step selection of optimization, and the spatial optimization process are all similar. In other words, these algorithms both perform a global search in a certain space and gradually reduce the range during the search process, while gradually tending towards the optimal value. Regardless whether the form of the solution is for a reduction in temperature or for a bird looking for food, these algorithms can be summarized as the macroscopic form of space mobile optimization. The difference is that these two methods are based on different physical theories, different specific functions, different search processes, and different parameter controls.

Comparing the computational times used in the above four methods, it can be found that the GA takes the least amount of time, while the SA takes the longest amount of time. Although the BH-PSO requires less time than the PSO, it still does not reach the efficiency of the GA. When taking into account the differences in results and truth values of different methods, the BH-PSO can obtain more accurate results than the GA, and the time taken is shorter than that taken by the SA. An overall analysis of the BH-PSO indicates that it is more conducive to practical operations. At the same time, the several inversion algorithms mentioned above can obtain the solutions of the approximate true values to some extent, which indicates that the above algorithms all have the ability to resist errors and are suitable for inverting volcanic pressure source parameters. By comparison, it can be found that the accuracy of the BH-PSO algorithm is higher than that of the PSO algorithm, which indicates that the improved strategy in this paper is correct and reasonable. Introducing the radius of the black hole into the PSO helps to improve

the ability of PSO to overcome local minima, and thus, the search speed depends on intelligent changes of during the actual search process. The intelligent changes to the actual process reduce the possibility of falling into local minima and improve the success rate of the inversion. This is in accordance with the original intention of introducing the black hole strategy to PSO in this paper and achieves the intended purpose of improving the PSO algorithm.

4.2. BH-PSO + Yang

In the simulation experiment of the Yang model, a volcanic eruption event was simulated on a domain of 20 km × 20 km with the center of the volcanic eruption projected onto the surface of the Earth as the origin. The preset true values of the simulated parameters are shown in Table 2. The displacements obtained after the forward modeling are converted into deformation observation data in the InSAR viewing direction (observation azimuth of ascending orbit is −10°, radar wave incidence angle of 23°) and its observations are inverted by adding errors following a normal distribution (with a mean of 0 and a magnitude of 0.5 cm). To verify the effectiveness and efficiency of the proposed method, the SA, GA, PSO and BH-PSO methods are also used to invert the above Yang model observations with different errors.

Fig. 6(a) indicates that that the InSAR-observed deformation values are no errors under the preset true values, (b) indicates that the InSAR-observed deformation values are obtained after adding error of 0.5 cm, (c) is the simulation result using the GA method, (d) is the SA method simulation result (e) is the PSO method simulation result (f) is the BH-PSO method simulation result. (g) is the residual of SA method inversion, (h) is the residual of GA method inversion, (i) is the residual of PSO method inversion, (j) is the residual of BHPSO method inversion

The results of this experiment show that the results obtained by BH-PSO is the best under the RMSE index, followed by the SA, and the worst by the GA. The simulation results show that the reliability of the GA method is poor when using Yang model for volcanic inversion. At the same time, in the simulation experiments, this paper finds that when Yang model is solved, the selection of pressure parameters has a great impact on the results. Therefore, in actual operation, geological information should be combined to determine the correct and suitable
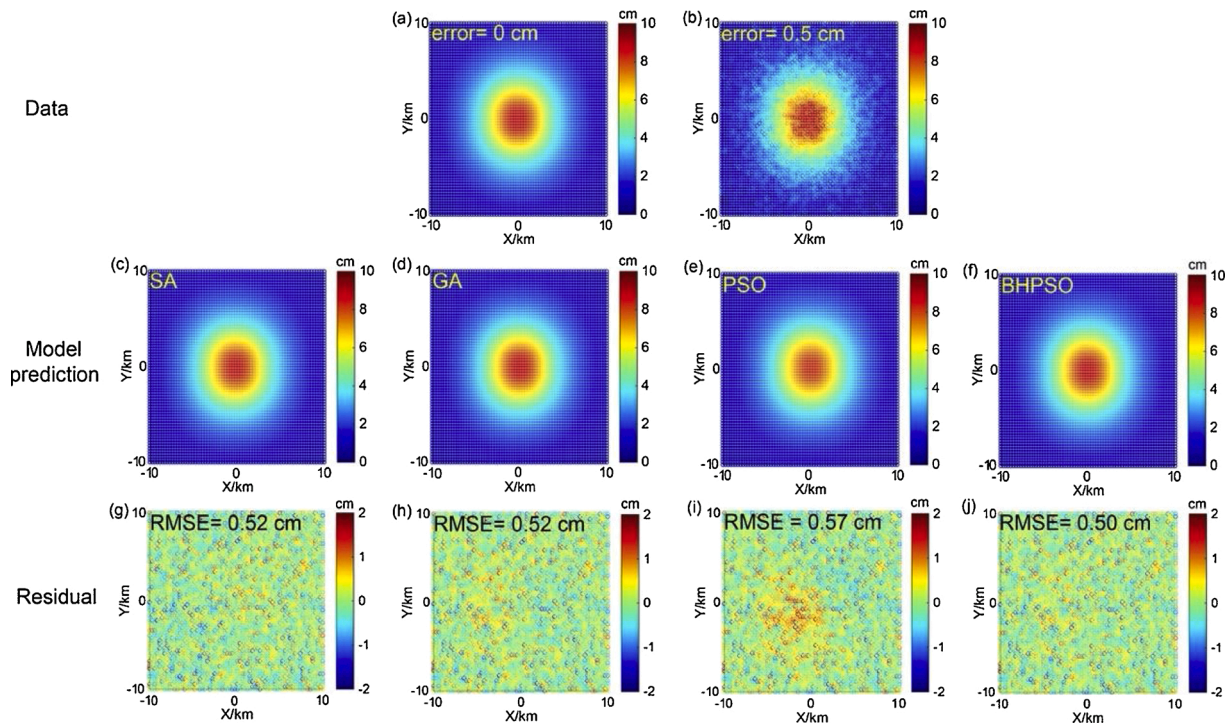
Fig. 5. Simulation experiment observation chart of Mogi model.

Table 2
Search intervals of input parameters (Yang) and inversion results using different methods.

	X/km	Y/km	D/km	a/km	b/km	Plunge/(°)	Trend/(°)	RMSE cm
Truth	0	0	5	1	0.5	45	45	/
GA	0.01	0.00	5.05	1.07	0.53	44.14	44.59	0.50
SA	0.05	−0.03	5.07	1.03	0.52	43.28	44.31	0.82
PSO	0.01	−0.01	5.02	0.96	0.47	44.80	45.96	0.68
BH-PSO	0.01	0.01	5.00	0.97	0.49	44.54	45.17	0.36

Note: In this model, the Poisson's ratio is 0.25, the shear modulus is 5 GPa. In this experiment, the pressure-related parameter P is set to a fixed value (in Eq.10), and it is treated as a constant in the inversion.

pressure parameters, and substitute them into the Yang model as a fixed solution. Through this simulation experiment, the applicability of the method in this paper is verified.

4.3. BH-PSO + CDM

In the simulation experiment of the CDM, a volcanic eruption event was simulated on a domain of 20 km × 20 km with the center of the volcanic eruption projected onto the surface of the Earth as the origin. The preset true values of the simulated parameters are shown in Table 3. The parameters are substituted into the CDM of a single pressure source for forward modeling. The displacements obtained after the forward modeling are converted into deformation observation data in the InSAR viewing direction observation azimuth of ascending orbit is -10°, radar wave incidence angle of 23°) and its observations are inverted by adding errors following a normal distribution (with a mean of 0 and a magnitude of 0.5 cm). To verify the effectiveness and efficiency of the proposed method, the SA, GA, PSO and BH-PSO methods are also used to invert the above CDM observations with different errors.

Fig. 7(a) indicates that that the InSAR-observed deformation values are no errors under the preset true values, (b) indicates that the InSAR-observed deformation values are obtained after adding error of 0.5 cm, (c) is the simulation result using the SA method, (d) is the GA method simulation result (e) is the PSO method simulation result (f) is the BH-

PSO method simulation result. (g) is the residual of SA method inversion, (h) is the residual of GA method inversion, (i) is the residual of PSO method inversion, (j) is the residual of BHPSO method inversion.

The results recorded in Table 3 show that under the more complicated CDM. The SA, GA, PSO and BH-PSO algorithms, solutions close to the true value can be obtained to a certain extent, but none of these algorithms can obtain the optimal values of all 9 parameters simultaneously. When the RMSE is used as the criterion, the BH-PSO algorithm has the best effect. However, the RMSE alone cannot be used to identify which algorithm has the highest accuracy. This paper considers that the CDM contains both angle unit parameters and length unit parameters, and the units of these two parameters are inconsistent. If the units are compared, problems will arise. Therefore, this paper designs an experiment to investigate the parameter sensitivity in the CDM. The experimental results are as follows:

Through experiments, this paper believes that in the CDM, the influence of the error in the angle is small, while the length error of a, b and c axes with strong correlation with volume has a great influence on the inversion result. Finally, this paper believes that the inversion results and the true values of the BH-PSO algorithm deviate to some degree, but the residuals reflected by the RMSE have a certain relationship with the magnitude of the error. The position and size of the magma source obtained by the algorithm and the volume of the magma source thus obtained are basically consistent with the real situation (the deviations
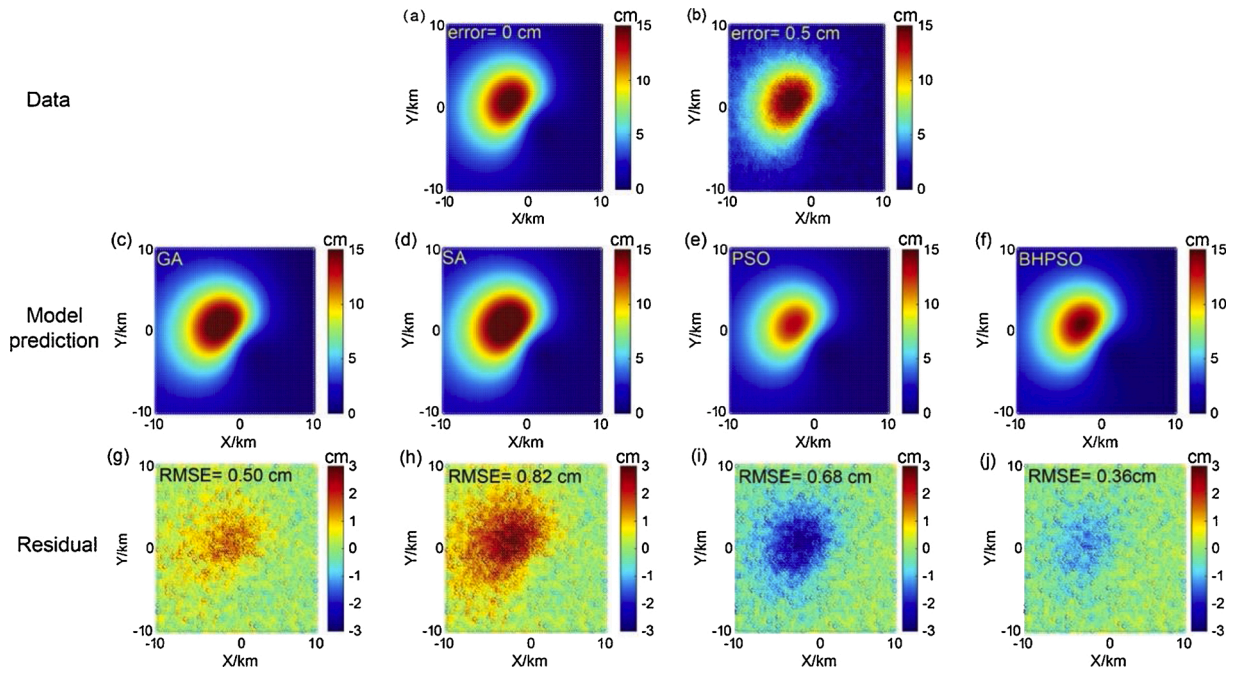
Fig. 6. Simulation experiment observation chart of Yang model.

Table 3
Search intervals of input parameters (CDM) and inversion results using different methods.

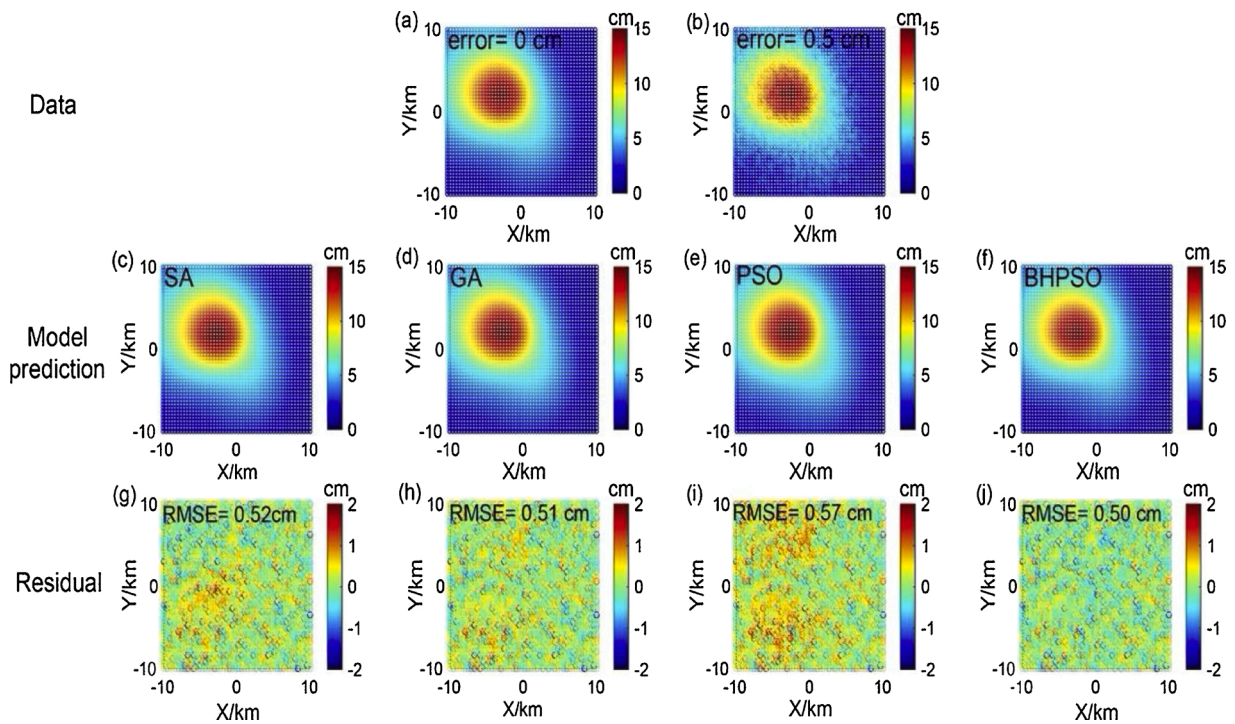|	X/km	Y/km	D/km	$\varphi_a/°$	$\varphi_b/°$	$\varphi_c/°$	a/km	b/km	c/km	RMSE cm
Truth	0	0	7	20	−15	45	0.3	1.2	0.8	/
GA	0.08	−0.10	6.97	20.75	−15.43	44.85	0.31	1.17	0.82	0.51
SA	0.05	0.16	6.92	18.95	−14.75	44.90	0.32	1.12	0.85	0.52
PSO	0.10	0.22	7.08	7.17	−14.80	44.97	0.32	1.15	0.87	0.57
BH-PSO	0.02	−0.03	6.99	21.82	−14.83	44.85	0.30	1.19	0.81	0.50

Fig. 7. Simulation experiment observations of CDM.

from the true values are small), and the shape of the chamber may have a small influence, but the result of the algorithm is still more realistic than the results of the Mogi model and the Yang model with only a single shape. Therefore, the BH-PSO method can be used for the parameter inversion of the CDM.

5. Inversion of the Calbuco volcanic pressure source parameters

5.1. Processing the InSAR data

InSAR has become an important means of acquiring observations of the Earth due to its many advantages, its high resolution and high precision under any weather condition, its wide coverage and its ability to discern vertical deformation compared with traditional GPS measurements. Because the deformation observations of volcanoes and earthquakes are often dynamic and large in scale and require a high precision, InSAR is one of the most commonly used sources of data to invert for the geometry and location of the magma chamber, the magma volume, the magma transport characteristics, and the magma eruption extent during volcanic activity (Dvorak and Dzurisin, 1997; Dzurisin, 2003; Dzurisin and Lu, 2007; Pinel et al., 2014; Xu et al., 2017). This article, considers the first eruption of the Calbuco volcano at 18:04 on April 22, 2015, the second eruption at 01:08 on April 23, and the third eruption on April 30. Therefore, the data used for this sequence of eruptions are InSAR data recorded on ascending and descending tracks after April 30 (after the volcanic eruption). In this paper, two partial images that effectively reflect the deformation due to the volcanic eruption are obtained by interferometry, and differentia and shear processing, as shown in Fig. 8.

It can be seen from Fig. 8 that there are deformation changes in the vicinity of the crater in both the ascending and the descending data, especially the LOS-A image, which clearly reveals the circular gradient of deformation. Compared with the descending data, the deformation revealed by the ascending data in the far field (for example, in the longitude range (-72°36′ ~ -72°24′), and the latitude range (−41°12′ ~ -41°00′) in subgraph a) is significantly reduced. However, the deformation in the LOS-D image near the crater is obviously weak, and thus, it is impossible to form a significant circular gradient of deformation. Since the cropped image still has a relatively large number of points (more than six million points), the inversion requires a considerable amount of time and a high computational complexity, and there are many interference points in the two subgraphs that are not conducive to the calculation. Therefore, this paper uses MATLAB software to process the raw image data on the quad-tree downsampling method (Jónsson et al., 2002; Wang et al., 2018a, b; Wang et al., 2019). This processing method not only can effectively preserve the deformation details, but also avoid far-field data redundancy. The quality of the downsampled results is effectively improved, the number of observation points is <3000 after resampling, and both images maintain the characteristics of

the originals after downsampling. Therefore, the following work in this paper will be carried out on the downsampled results.

5.2. Calbuco volcanic pressure source parameter inversion

In this paper, the characteristics of the deformation distribution in Fig. 8 are analyzed. A large deformation disturbance is considered in the far-field data of LOS-A image (the deformation variable is 0−1 cm at 20 km on the left side of the crater and >35 km on the right side of the crater). The magnitude of deformation reaches 4 cm, which is too large, and is inconsistent with the theoretical deformation of volcanic eruptions, moreover, the same position in the LOS-D image does not show such large deformation interference. Fig. 8 shows that the near-field deformation in the LOS-A image is significantly greater than that in the LOS-D image. However, LOS-D data are needed to constrain the far-field effect. If an inversion is performed for only the LOS-A data, the advantage would be that the crater position deformation could be fittied, but the effect may be poor for far-field data, and the single-source model may not be able to explain the far-field deformation in LOS-A image. Similarly, if only the LOS-D data are inverted, the effect may be more scattered and not well constrained. Therefore, to obtain more reasonable pressure source parameters, while balancing both the far-field and the near-field deformation, the Mogi model and CDM of a single pressure source are used to simultaneously reverse the deformation obtained after downsampling the LOS-A and LOS-D data. Using the Mogi model as an example, Eq (12) is employed

$$D_{los} = D_{los-A} + D_{los-D} \tag{12}$$

where D_{los-A} and D_{los-D} represent the simulated deformations in the LOS-A and LOS-D data, respectively, generated under a single-source Mogi model, and obtained by Eqs. (7) and (8); the standard used to evaluate the inversion results is Eq. (9), where D_{los} in Eq. (9) is the original LOS-A and LOS-D combined observation. When the result obtained by Eq. (9) is the smallest, the corresponding parameter values in Eq. (1), are sought as the solutions of the Mogi model.
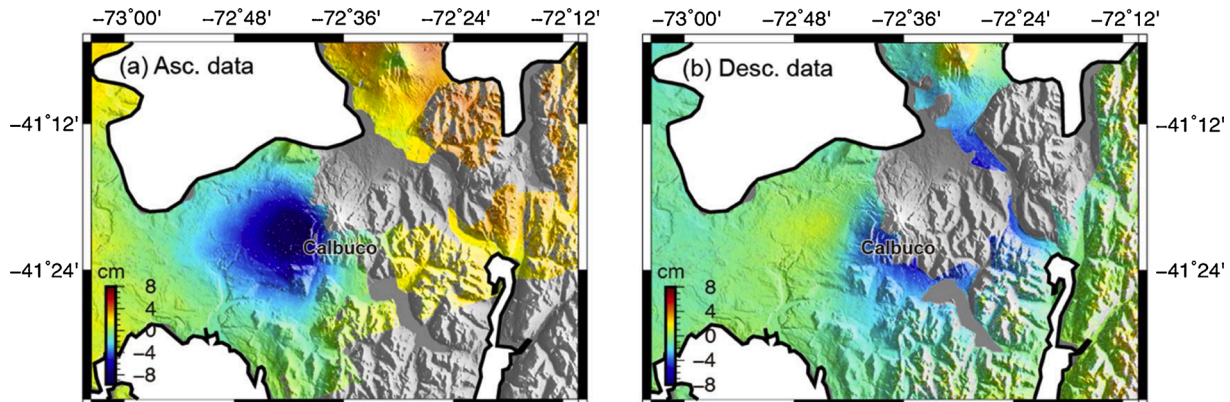
5.2.1. Inversion results based on a single-source Mogi model

Under the Mogi model, the parameter interval of Table 4 is selected

Table 4
Parameter search intervals and the inversion results using single Mogi pressure source.

	X/km	Y/km	D/km	$\Delta V/km^3$	RMSE(all) cm
Lower limit	30	25	6	0.03	/
Upper limit	50	45	12	0.8	/
LOS-A + D	40.951	30.056	8.627	0.345	1.80

Fig. 8. (a) Unwrapped ascending and (b) descending interferograms showing the LOS ground deformation associated with the 2015 Calbuco eruption.

using the BH-PSO algorithm to perform the inversion. The obtained results are forward-calculated (using the Mogi model), the obtained shape variables are converted into InSAR data shape variables according to Eq (2), and the transformed shape variables and original observation shape variables and residuals are plotted in Fig. 9.

As shown in Table 4, the position of the volcanic pressure source obtained by the inversion is (X: 40.951 km, Y: 30.056 km), the position of the crater is (X: 47 km, Y: 35 km), and the position of the obtained magma chamber is near the crater within 5−7 km, at depth of 8−9 km below the surface. The results of this paper are consistent with those of Delgado et al. (2017), which means that the depth of the magma chamber is similar numerically. Which is different from the petrological and geochemical methods used by Arzilli et al. (2019) and Namur et al. (2020), the data used in this paper and Delgado et al. (2017) are geodetic data and the mogi model. The comparison between the results of this paper and Delgado et al. (2017) is to verify that the accuracy of BH-PSO method is higher than that of GA and SA methods. Different

from Arzilli et al. (2019); Namur et al. (2020) and Morgado et al. (2019), geodesy inversion method is used in this paper. Although this method is different from petrology and geochemistry in theory, the results of different literatures are all around 8 km. Therefore, the results of this paper have credibility. At the same time, in Table 7, the research results are discussed in detail in this paper. After a comparative analysis, this paper finds that the single pressure source model can better invert the Ascending deformation data than the other algorithms. The direct result is that the model shape variable in Fig. 8 is close to the Ascending shape variable. Except for the large residuals of 3−4 cm in the far field, the residuals of the near-field data are ±2 cm, and the RMSE = 1.7 cm; however, the residuals in the Descending data indicate that difference between the model and data is large. The original Descending image contains a shape variable of -5 cm near the crater, and the residual of the inversion result is 6 cm. This produces a simulation result far exceeding the original shape variable, which indicates a single pressure source simulation, and the RMSE = 1.9 cm. The result of the model in the
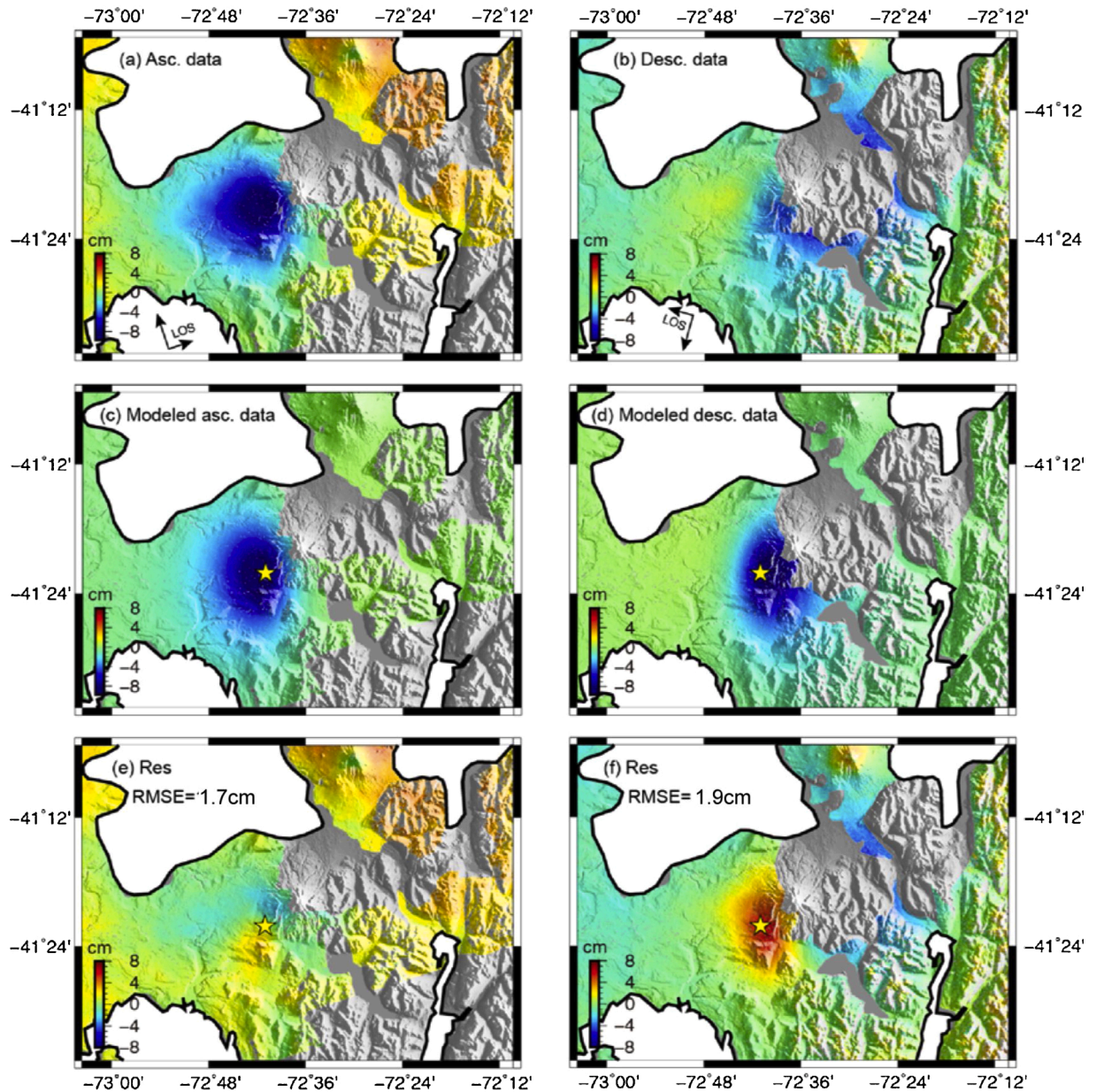

Fig. 9. Comparison of LOS ground deformation and the modeling results using a single the Mogi model. (a) and (b) represent the observed ascending and descending LOS deformation maps, respectively. (c) and (d) model predictions for panel (a) and (b) with the surface projection of the source indicated by a yellow star. (e) and (f) represent the Residuals.

Descending image is inaccurate, indicating that the Descending inversion results of the single-source Mogi model in is not ideal are not ideal. The mogi model is a widely used model, and the uncertainty of its results comes from two aspects: 1, The model is relatively simple, which simplifies the magma chamber to a standard sphere, which may be inconsistent with the actual situation; 2, the uncertainty of inversion methods, inversion accuracy of different methods is different. However, the BH-PSO method has been proved to have a relatively high accuracy in the simulation experiments. Therefore, the uncertainty in this paper is more caused by the model. Compared with parts 5.2.2 and 5.2.3, the CDM model can be more consistent with the actual distribution of the magma chamber.

5.2.2. Inversion results based on Yang models

Based on the above analysis, this paper use Eq. (12) and the Yang model to simultaneously invert the deformation obtained by Ascending and Descending in Fig. 8. The specific parameter search interval of the inversion is shown in Table 5. The BH-PSO algorithm proposed in this paper is adopted, and the obtained parameter results are recorded in Table 5. The parameter values of the different inversion results are forward-calculated based on the Yang model, the shape variables obtained by the forward calculation are converted into InSAR data according to Eq.(8), and the transformed shape variables (the inversion results), the original observation shapes variables and residuals are plotted in Fig. 10.

The results in Table 5 show the position of pressure source (X: 44.871 km, Y: 37.830 km) obtained under the dual pressure source model, and the buried depth is D: 8.151 km. This result is similar to the results in Table 7. These inversion results are consistent with the results of Delgado et al. (2017), indicating the correctness of pressure source. The depth before magma eruption has been more discussed in petrology and chemistry, for example in Arzilli et al. (2019); Namur et al. (2020); Morgado et al. (2019). Geodetic data are obtained from the deformation before and after eruption, under which it is difficult to infer the mechanism of the magma chamber before eruption. The depth discussed here is derived from a combination of geodetic deformation and magmatic models. The heating, supply, and pressure changes of the magma before the volcanic event are difficult to reflect in the InSAR data. Therefore, this paper agrees with the explanations of Arzilli et al. (2019); Namur et al. (2020); Morgado et al. (2019); Pardini et al. (2018) for the temperature change, pressure change and magma chamber heating mechanism before the occurrence of volcanic. In Fig. 10, the pressure source of Yang Model can better reflect the deformation of the descending rail, but the deformation of the ascending rail is not improved. The descending residual in Fig. 10 indicates that the simulated value near the crater is close to the original derailment data, with a residual of 0−2 cm, which is much smaller than the 6 cm residual in Fig. 9 (and significantly more improve). However, there is still a 4 cm deviation in the area away from the crater in the ascending rail, the fitting result of the ascent is not good enough, and the RMSE is still large. Combining the two images data, the results of the Yang model are better than the Mogi model, and the derailment data is significantly improved. However, the RMSE (1.30 cm) of the Yang model is still bigger than the RMSE of the CDM (RMSE = 1.14 cm). Therefore, according to the data fitting results, the results of CDM are more reliable. Therefore, this paper is more inclined to the results of CDM.

5.2.3. Inversion results based on a single CDM

The parameter settings and inversion results of the CDM model are shown in Table 6. The transformed shape variables (inversion results) are compared with the original observed shape variables and the residuals are plotted in Fig. 11.

The position of the volcanic pressure source obtained by the inversion in Table 6 is (X: 46.511 km, Y: 34.511 km), the position of the crater (X: 47 km, Y: 35 km), and the position of the obtained magma chamber is near crater 2 within the range of 3 km, at a depth of less than 9 km below the surface. The above results (depth, a, b, c) are similar to those of Nikkhoo et al. (Nikkhoo et al., 2016); About the pre-eruptive depth, this paper is similar with Nikkhoo et al. (Nikkhoo et al., 2016), the difference is within 1 km. The reason for this difference may be the difference between observed data and inversion methods. After a comparative analysis, this paper finds that the CDM can better invert the LOS-A deformation data. The direct result is that in Fig. 11, the LOS-A shape variable of the Model is close to the Ascending Data, and thus, the Residual of Ascending is reduced overall, however, there are large residuals of 3−4 cm in the far field, and relatively small residuals of ±1 cm in the near-field. Furthermore, the Descending result is also very similar, and the magnitudes of the residuals are in the range of -2 to 0 cm (for the Descending near-field). This result is significantly reduced compared to the residual of -6 cm in Fig. 9 This finding shows that the CDM in Fig 12 produces more obvious deformation than the Descending effect in the Mogi model in Fig. 9, that is, the inversion result of the CDM is closer to the original data than the inversion result of the Mogi model.

According to the research results of Ragon et al. (2018), this paper considers that the RMSE (all) in Tables 3, 4, and 5 are comparative, because the data volumes of the three models are consistent with their data quality, however, the models themselves are different. Such a result can reflect the quality of the model, and the results show that the CDM has a better effect on the data fit. However, compared with the existing research results, the CDM provides of the magma eruption and the pressure source, will be large differences (which is a limitation of the algorithm itself). Experiments 4 also shows that the inverted results of the CDM for the magma emissions are smaller than those of the Mogi model. This discrepancy is independent of the image data and is a computational problem of the CDM itself.

Based on the above analysis, the results of the CDM are more consistent with the fitted shape variable for this eruption event. However, there is a certain amount of deviation between the estimated magma emissions and the estimated pressure source position; the deviation in the pressure source position is approximately 3 km, which is an acceptable range, and the magma emissions are slightly reduced. Through 30 independent inversion experiments and the obtained statistical information, this paper speculates that the total volume of the erupted volcanic material in the Mogi model is 0.345 km^3, and the pressure source is located near the crater. Under the CDM, the total volume of erupted volcanic material eruptions is between 0.209 km^3, and the pressure source is also located near the crater (within 1.5 km in the X direction, and within an offset range of 1 km in the Y direction). These depth results are close to the Mogi model.

In the Table 7, the superscript [M] represents the inversion result of the Mogi model, and the superscript [C] represents the inversion result of the CDM. Table 7 records the results reported by different researchers on the volume of erupted material and the location and depth of the pressure
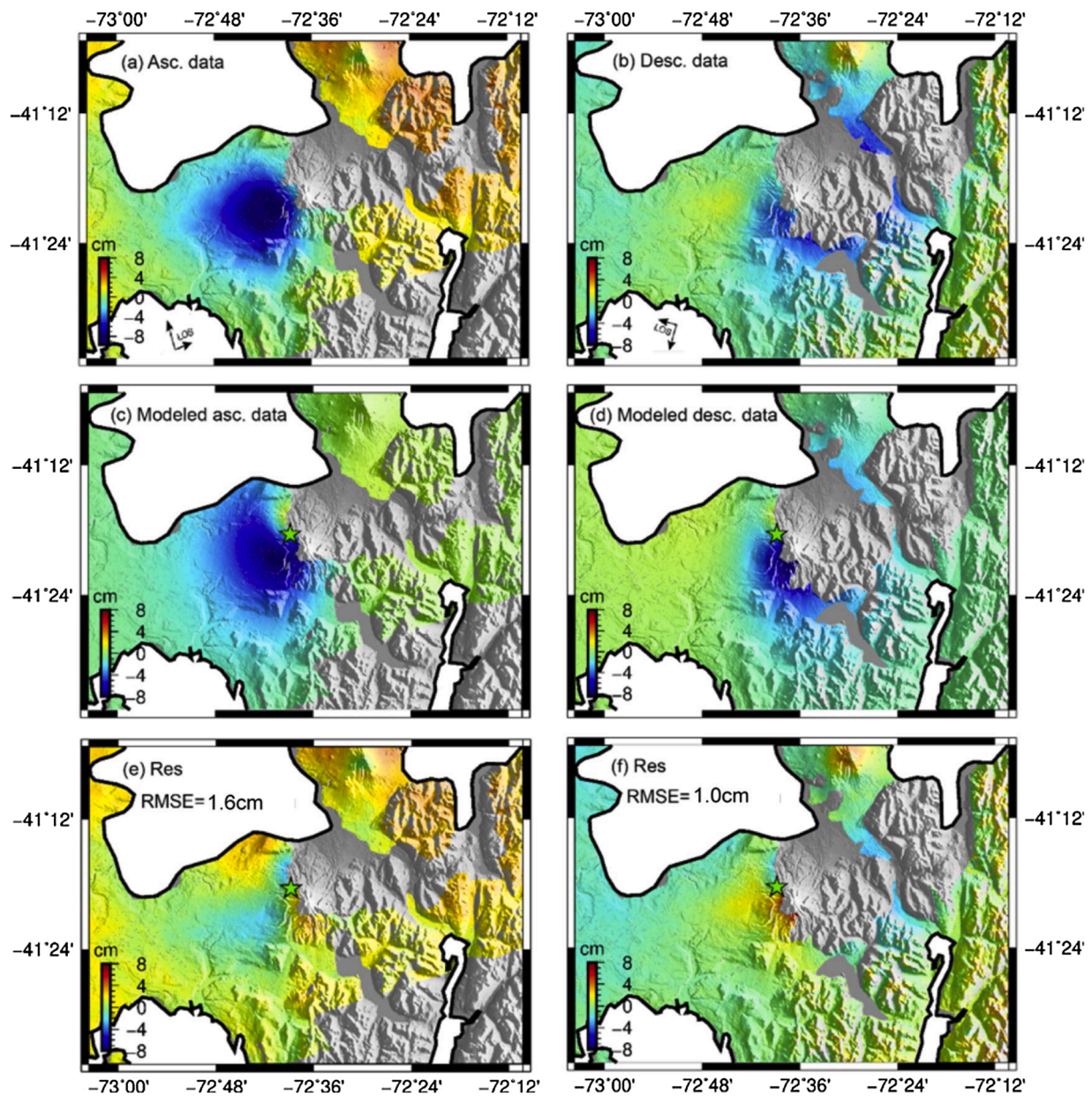
Table 5
Parameter search intervals and the inversion results using Yang pressure source.

	X/km	Y/km	D/km	a/km	b/km	Plunge/(°)	Trend/(°)	RMSE(all) cm
Lower limit	30	20	10	0.2	0.1	0	250	/
Upper limit	55	50	20	2	2	90	360	/
LOS-A + D	44.871	37.830	8.151	1.473	0.742	16.738	282.066	1.30

Note: In this model, the Poisson's ratio is 0.25, the shear modulus is 5 GPa (Delgado et al., 2017).

Fig. 10. Same as Fig. 9, but for the Yang source model. The green star represent the location of Yang sources.

Table 6
Parameter search intervals and the inversion results using the CDM model.

	X/km	Y/km	D/km	$\varphi_a/°$	$\varphi_b/°$	$\varphi_c/°$	a/km	b/km	c/km	$\Delta V/km^3$	RMSE(all) cm
Lower limit	30	25	6	−10	−15	145	0	0	0	/	
Upper limit	50	45	12	10	5	170	1	3	3	/	
LOS-A + D	46.511	34.511	9.035	1.989	−5.469	153.027	0.325	1.228	1.429	0.209	1.14

source. By comparison, it can be found that the results of this study are within the scope of existing research results. The research results of this paper are closer to the results of Castruccio (2016) and Van Eaton et al. (2016); Morgado et al. (2019); Delgado et al(2017), and Pardini et al. (2018) think that assuming a magma density of ~2500 kg m^{-3}, they compute a deposit dense rock equivalent (DRE) of 0.198 ± 0.050 km^3, and the total erupted volume has been estimated 0.48 km^3. The source depth is similar to that of Delgado et al. (2017); the difference is that Delgado (2017) used both the Mogi model and the Yang model. This

paper read the results of Delgado et al. (2017); Arzilli et al. (2019); Morgado et al. (2019), and Namur et al. (2020), of which Morgado et al. (2019) showed a range of 5–9.5 km. However, the results from Delgado et al. (2017); Arzilli et al. (2019) and Namur et al. (2020) show that the pre-restraint depth is 8−12 km, which is close to the 9 km in this paper. The above results are obtained on the basis of different geophysical research methods, different models and inversion methods. This also leads to different depths of the same volcanic event. It is worth noting that the depth of 9 km obtained in this paper is the approximate median
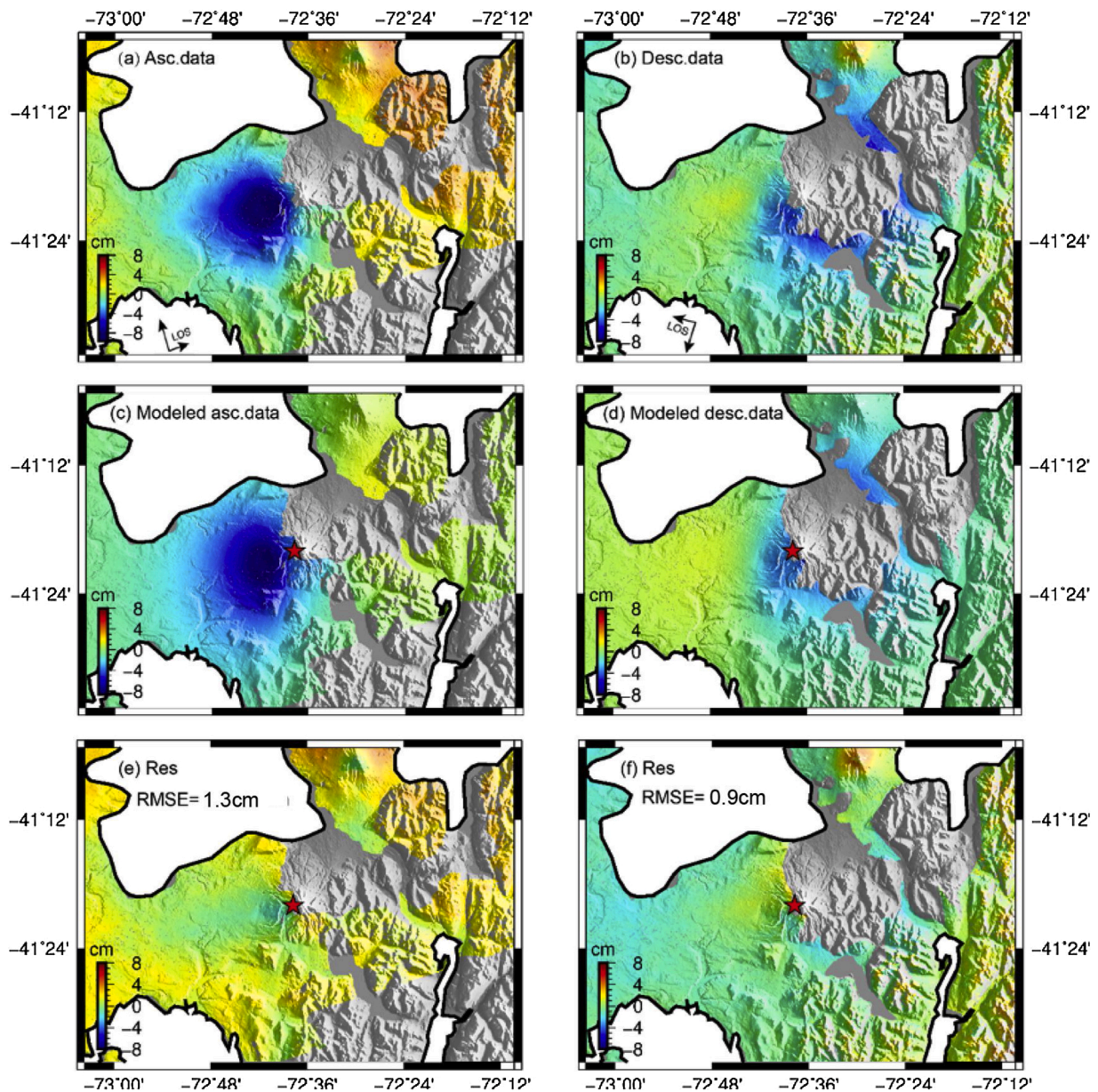
Fig. 11. Same as Fig. 9, but for the CDM source model. The red star represents the centroid of CDM.

Table 7
Comparison of different inversion results from the existing studies and this work.

	X/km	Y/km	D/km	$\Delta V/km^3$
This paper	$^M40.95$ $^C46.05$	30.06 34.51	8.63 9.05	0.345 0.209
Romero et al. (2016)	/	/	/	0.27 ± 0.007
Van Eaton et al 2016	/	/	/	0.56 ± 0.28
Castruccio et al 2016	/	/	/	0.38 ± 0.1
Nikkhoo(2017)	/	/	8.2	0.1
Arzilli et al. (2019)	/	/	8–12	/
Morgado et al. (2019)	/	/	5.5–9.5	0.3–0.6
Namur et al. (2020)	/	/	8–11	0.27–0.6
Pardini et al. (2018)	/	/	/	0.48
Delgado et al (2017)	699.2 ± 0.2 696.3 ± 0.3	5419.0 ± 0.3 5419.4 ± 0.2	7.78 ± 0.3 10.7 ± 0.4	0.37–0.6

of these research results, which is of reference significance.

Although the results of this paper and Delgado et al. (2017) all originate from two sets of parameters, the parameters between the Mogi model and the CDM used in this paper are inconsistent. Delgado et al. (2017) used WGS84UTM18S data, which resulted in different solutions for the X and Y coordinates. However, the pressure source parameters of the two models are close to the volcanic eruption port, so the results are credible. This paper believes that the interpretation of this volcanic eruption event has not been comprehensive, which is also related to the accuracy and quality of the data. Gaps in the data has a certain influence on the interpretation of volcanic movements. At the same time, the timeliness of the data is also a constraint. In areas with a high elevation, and complex vegetation and various vegetation types, the accuracy of InSAR data will be affected. However, the results of this paper still have a certain reference value. The method and explanation presented in this paper are applicable to the data in this paper.

6. Conclusion

This paper proposes a particle swarm optimization algorithm combined with black hole strategy (the BH-PSO algorithm). By applying the radius selection strategy of the black hole algorithm to the weighted selection of the step size in the particle swarm optimization algorithm, the two approaches are combined. The BH-PSO algorithm can dynamically adjust the moving distance and moving direction of the particles in each iteration according to the ratio of the fitness of the global optimal solution to the fitness of the individual optimal solution during the search process. This dynamic adjustment strategy is more intelligent than the monotonically increasing or decreasing strategies adopted in previous studies. This intelligent adjustment method can obtain the global optimal solution more quickly and accurately within the solution space of the parameters; and solves the problem that the result of the artificial interference step size of the particle swarm algorithm easily to misses the global optimum and becomes trapped in local minima. The theoretical analysis and simulation experiments prove that the BH-PSO algorithm is effective and practical in the inversion of volcanic pressure source parameters. The experimental results show that the improved particle swarm optimization algorithm overcomes the local optima problem to some extent, the global optimum is achieved, and the PSO algorithm boasts an improved accuracy and efficiency. The results show that the CDM will underestimate the volume of erupted magma to a certain extent. However, with the RMSE as the evaluation index, the effect of the CDM is better than that of the Mogi model. Moreover, that the results of the CDM are more consistent at fitting the shape variable than the Mogi model. In the CDM, the pressure source position is near the crater, while the depth is close to the estimate from the Mogi model (approximately 9 km below the surface). The total volume of erupted volcanic material obtained under the CDM is 0.209 km^3, which will underestimate the volcanic eruption volume. This paper agrees with the 0.345 km^3 obtained by the Mogi model. However, the mechanisms of underground magma connection system, magma supply and underground movements for volcanic events cannot be clearly determined, but the results of the dual pressure source Mogi model may provide some reference value. At the same time, the data used in this paper contain some missing data, and the InSAR data are greatly affected atmosphere and by the presence of vegetation and volcanic ash. Therefore, the results obtained in this paper do not correspond to the ideal data constraint acquisition state, and thus, there will be a certain amount of deviation.

Author statement

We declare that we have no financial and personal relationships with other people or organizations that can inappropriately influence our work, there is no professional or other personal interest of any nature or kind in any product.

Declaration of Competing Interest

We declare that we have no financial and personal relationships with other people or organizations that can inappropriately influence our work, there is no professional or other personal interest of any nature or kind in any product, service and/or company that could be construed as influencing the position presented in, or the review of, the manuscript entitled,

Acknowledgements

References

Arzilli, F., Morgavi, D., Petrelli, M., et al., 2019. The unexpected explosive sub-Plinian eruption of Calbuco volcano (22–23 April 2015; Southern Chile): triggering mechanism implications. J. Volcanol. Geotherm. Res. 378, 35–50. https://doi.org/10.1016/j.jvolgeores.2019.04.006.

Castruccio, A., Clavero, J., Segura, A., et al., 2016. Eruptive parameters and dynamics of the April 2015 sub-Plinian eruptions of Calbuco volcano (southern Chile). Bull. Volcanol. 78 (9), 62. https://doi.org/10.1007/s00445-016-1058-8.

Chen, G.H., Shan, X.J., Moon, W.M., et al., 2008. A modeling of the magma chamber beneath the Changbai Mountains volcanic area constrained by InSAR and GPS derived deformation. Chin. J. Geophys. 51 (4), 765–773. https://doi.org/10.1002/cjg2.1269.

Delgado, F., Pritchard, M.E., Ebmeier, S., et al., 2017. Recent unrest (2002–2015) imaged by space geodesy at the highest risk Chilean volcanoes: villarrica, Llaima, and Calbuco (Southern Andes). J. Volcanol. Geotherm. Res. 344, 270–288. https://doi.org/10.1016/j.jvolgeores.2017.05.020.

Dvorak, J.J., Dzurisin, D., 1997. Volcano geodesy. The search for magma reservoirs and the formation of eruptive vents. Rev. Geophys. 35 (3), 343–384. https://doi.org/10.1029/97rg00070.

Dzurisin, D., 2003. A comprehensive approach to monitoring volcano deformation as a window on the eruption cycle. Rev. Geophys. 41 (1) https://doi.org/10.1029/2001rg000107.

Dzurisin, D., Lu, Z., 2007. Interferometric Synthetic-aperture Radar (InSAR) //Volcano Deformation. Springer, Berlin, Heidelberg, pp. 153–194. https://doi.org/10.1007/978-3-540-49302-05.

Eberhard, R., Kennedy, J., 1995. A new optimizer using particle swarm theory//MHS'95. Proceedings of the Sixth International Symposium on Micro Machine and Human Science 39–43. https://doi.org/10.1109/mhs.1995.494215.

Ebmeier, S.K., 2016. Application of independent component analysis to multitemporal InSAR data with volcanic case studies. J. Geophys. Res. Solid Earth 121 (12), 8970–8986. https://doi.org/10.1002/2016JB013765.

Feng, W.P., Li, Z.H., 2010. A novel hybrid PSO/simplex algorithm for determining earthquake source parameters using InSAR data. Progress in Geophysics 25 (4), 1189–1196. https://doi.org/10.3969/j.issn.1004-2903.2010.04.007.

Fialko, Y., Khazan, Y., Simons, M., 2001. Deformation due to a pressurized horizontal circular crack in an elastic half-space, with applications to volcano geodesy. Geophys. J. R. Astron. Soc. 146 (1), 181–190. https://doi.org/10.1046/j.1365-246X.2001.00452.x.

Gambino, S., Guglielmino, F., 2008. Ground deformation induced by geothermal processes: a model for La Fossa crater (Vulcano Island, Italy). J. Geophys. Res. Solid Earth 113 (B7). https://doi.org/10.1029/2007jb005016.

Ghamisi, P., Couceiro, M.S., Martins, F.M.L., et al., 2014. Multilevel image segmentation based on fractional-order darwinian particle swarm optimization. IEEE Trans. Geosci. Remote. Sens. 52 (5), 2382–2394. https://doi.org/10.1109/tgrs.2013.2260552.

Gong, M., Cai, Q., Chen, X., et al., 2014. Complex network clustering by multiobjective discrete particle swarm optimization based on decomposition. IEEE Trans. Evol. Comput. 18 (1), 82–97. https://doi.org/10.1109/tevc.2013.2260862.

Hatamlou, A., 2013. Black hole: a new heuristic optimization approach for data clustering. Inf. Sci. 222, 175–184. https://doi.org/10.1016/j.ins.2012.08.023.

He, S., Prempain, E., Wu, Q.H.A., 2004. N improved particle swarm optimizer for mechanical design optimization problems. Eng. Optim. 36 (5), 585–605. https://doi.org/10.1080/03052150410001704854.

Hotta, K., Iguchi, M., Ohkura, T., et al., 2017. Magma intrusion and effusion at Sinabung volcano, Indonesia, from 2013 to 2016, as revealed by continuous GPS observation. J. Volcanol. Geotherm. Res. https://doi.org/10.1016/j.jvolgeores.2017.12.015.

Ivy, D.J., Solomon, S., Kinnison, D., et al., 2017. The influence of the Calbuco eruption on the 2015 Antarctic ozone hole in a fully coupled chemistry-climate model. Geophys. Res. Lett. 44 (5), 2556–2561. https://doi.org/10.1002/2016GL071925.

Ji, L., Izbekov, P., Senyukov, S., et al., 2018. Deformation patterns, magma supply, and magma storage at Karymsky Volcanic Center, Kamchatka, Russia, 2000–2010, revealed by InSAR. J. Volcanol. Geotherm. Res. 352, 106–116. https://doi.org/10.1016/j.jvolgeores.2018.01.011.

Jónsson, S., Zebker, H., Segall, P., et al., 2002. Fault slip distribution of the 1999 M w 7.1 Hector Mine, California, earthquake, estimated from satellite radar and GPS measurements. Bull. Seismol. Soc. Am. 92 (4), 1377–1389. https://doi.org/10.1785/0120000922.

Lara, L.E., Orozco, G., Amigo, A., et al., 2011. Peligros Volcánicos de Chile. Servicio Nacional de Geología y Minería. Carta Geológica de Chile. Serie Geología Ambiental 13, 34.

Liu, X., Zhang, Q., Shah, M., et al., 2017. Atmospheric-ionospheric disturbances following the April 2015 Calbuco volcano from GPS and OMI observations. Adv. Space Res. 60 (12), 2836–2846. https://doi.org/10.1016/j.asr.2017.07.007.

Matoza, R.S., Fee, D., Green, D.N., et al., 2018. Local, regional, and remote seismo-acoustic observations of the April 2015 VEI 4 eruption of Calbuco volcano, Chile. J. Geophys. Res. Solid Earth 123 (5), 3814–3827. https://doi.org/10.1002/2017JB015182.

Mogi, K., 1958. Relations between the eruptions of various volcanoes and the deformations of the ground surfaces around them. Bull. Earthquake Res. Inst. Univ. Tokyo 36, 99–134.

Morgado, E., Morgan, D.J., Harvey, J., et al., 2019. Localised heating and intensive magmatic conditions prior to the 22–23 April 2015 Calbuco volcano eruption (Southern Chile). Bull. Volcanol. 81 (4), 24.

Namur, O., Montalbano, S., Bolle, O., et al., 2020. Petrology of the April 2015 eruption of Calbuco volcano, southern Chile. J. Petrol. https://doi.org/10.1093/petrology/egaa084.

Nikkhoo, M., Walter, T.R., Lundgren, P.R., et al., 2017. Compound dislocation models (CDMs) for volcano deformation analyses. Geophys. J. Int. 208 (2), 877–894. https://doi.org/10.1093/gji/ggw427.

Nunnari, G., Puglisi, G., Guglielmino, F., 2005. Inversion of SAR data in active volcanic areas by optimization techniques. Nonlinear Process. Geophys. 12 (6), 863–870. https://doi.org/10.5194/npg-12-863-2005.

Pardini, F., Burton, M., Arzilli, F., La, Spina, et al., 2018. SO2 emissions, plume heights and magmatic processes inferred from satellite data: the 2015 Calbuco eruptions. J. Volcanol. Geotherm. Res. 361, 12–24. https://doi.org/10.1016/j.jvolgeores.2018.08.001.

Pinel, V., Poland, M.P., Volcanology, Hooper A., 2014. Lessons learned from synthetic aperture radar imagery. J. Volcanol. Geotherm. Res. 289, 81–113. https://doi.org/10.1016/j.jvolgeores.2014.10.010.

Ragon, T., Sladen, A., Simons, M., 2018. Accounting for uncertain fault geometry in earthquake source inversions–I: theory and simplified application. Geophys. J. Int. 214 (2), 1174–1190. https://doi.org/10.1093/gji/ggy187.

Ratnaweera, A., Halgamuge, S.K., Watson, H.C., 2004. Self-organizing hierarchical particle swarm optimizer with time-varying acceleration coefficients. IEEE Trans. Evol. Comput. 8 (3), 240–255. https://doi.org/10.1109/tevc.2004.826071.

Romero, J.E., Morgavi, D., Arzilli, F., et al., 2016. Eruption dynamics of the 22–23 April 2015 Calbuco Volcano (Southern Chile): analyses of tephra fall deposits. J. Volcanol. Geotherm. Res. (317), 15–29. https://doi.org/10.1016/j.jvolgeores.2016.02.027.

Sangeetha, S.K., Sivakumar, V., Gebreslasie, M., 2018. Long-range transport of SO2 over South Africa: a case study of the Calbuco volcanic eruption in April 2015. Atmos. Environ. (185), 78–90. https://doi.org/10.1016/j.atmosenv.2018.04.056.

Sha, D.Y., Hsu, C.Y.A., 2008. New particle swarm optimization for the open shop scheduling problem. Comput. Oper. Res. 35 (10), 3243–3261. https://doi.org/10.1016/j.cor.2007.02.019.

Shi, Y.H., Eberhart, R.C., 1998. A modified particle swarm optimizer// evolutionary computation proceedings. IEEE World Congress on Computational Intelligence. The 1998 IEEE International Conference on. IEEE. https://doi.org/10.1109/icec.1998.699146, 1998.

Shi, X.M., Wang, J.Y., 2008. Genetic algorithm method. Chin. J. Eng. Geophys. 5 (2), 129–140. https://doi.org/10.3969/j.issn.1672-7940.2008.02.001.

Shi, X.M., Xiao, M., Fan, J.K., et al., 2009. The damped PSO algorithm and its application for magnetotelluric sounding data inversion. Chin. J. Geophys. 52 (4), 1114–1120. https://doi.org/10.3969/j.issn.00015733.2009.04.029.

Shirzaei, M., Walter, T.R., 2009. Randomly iterated search and statistical competency as powerful inversion tools for deformation source modeling: application to volcano interferometric synthetic aperture radar data. J. Geophys. Res. Solid Earth 114 (B10). https://doi.org/10.1029/2008jb006071.

Siebert, L., Simkin, T., Kimberly, P., 2011. Volcanoes of the World. Univ of California Press.

Stern, C.R., 2004. Active Andean volcanism: its geologic and tectonic setting. Revista geológica de Chile 31 (2), 161–206. https://doi.org/10.4067/s0716-02082004000200001.

Stone, K.A., Solomon, S., Kinnison, D.E., et al., 2017. Observing the impact of Calbuco volcanic aerosols on South Polar ozone depletion in 2015. J. Geophys. Res. Atmos. 122 (21) https://doi.org/10.1002/2017JD026987.

Tiampo, K.F., Rundle, J.B., Fernandez, J., et al., 2000. Spherical and ellipsoidal volcanic sources at Long Valley caldera, California, using a genetic algorithm inversion technique. J. Volcanol. Geotherm. Res. 102 (3–4), 189–206. https://doi.org/10.1016/s0377-0273(00)00185-2.

Van Eaton, A.R., Amigo, Á, Bertin, D., et al., 2016. Volcanic lightning and plume behavior reveal evolving hazards during the April 2015 eruption of Calbuco volcano, Chile. Geophys. Res. Lett. 43 (7), 3563–3571. https://doi.org/10.1002/2016GL068076.

Wang, L.Y., Yu, H., 2018. Application of total least squares joint adjustment to volcano inversion of mogi model. Geomatics Inf. Sci. Wuhan Univ. 43 (9), 1333–1341. https://doi.org/10.13203/j.whugis20160469.

Wang, L.Y., Gao, H., Feng, G.C., 2017. InSAR and GPS inversion for source parameters of the 2016 Mw6.4 Meinong, Taiwan earthquake. Chin. J. Geophys. 60 (7), 2578–2588. https://doi.org/10.6038/cjg20170707.

Wang, L.Y., Gao, H., Feng, G.C., et al., 2018a. Source parameters and triggering links of the earthquake sequence in central Italy from 2009 to 2016 analyzed with GPS and InSAR data. Tectonophysics (744), 285–295. https://doi.org/10.1016/j.tecto.2018.07.013.

Wang, L., Zhao, X., Gao, H., 2018b. A method for determining the regularization parameter and the relative weight ratio of the seismic slip distribution with multi-source data. J. Geodyn. 118, 1–10. https://doi.org/10.1016/j.jog.2018.04.005.

Wang, T., DeGrandpre, K., Lu, Z., et al., 2018c. Complex surface deformation of Akutan volcano, Alaska revealed from InSAR time series. Int. J. Appl. Earth Obs. Geoinf. 64, 171–180. https://doi.org/10.1016/j.jag.2017.09.001.

Wang, L., Zhao, X., Xu, W., et al., 2019. Co-seismic slip distribution inversion with unequal weighted Laplacian smoothness constraints. Geophys. J. Int. https://doi.org/10.1093/gji/ggz125.

Xu, W., Rivalta, E., Li, X., 2017. Magmatic architecture within a rift segment: Articulate axial magma storage at Erta Ale volcano, Ethiopia. Earth Planet. Sci. Lett. 476, 79–86. https://doi.org/10.1016/j.epsl.2017.07.051.

Yang, X., Davis, P.M., Dieterich, J.H.D., 1988. eformation from inflation of a dipping finite prolate spheroid in an elastic half-space as a model for volcanic stressing. J. Geophys. Res. Solid Earth 93 (B5). https://doi.org/10.1029/JB093iB05p04249.

Zhang, J., Liu, K., Tan, Y., et al., 2008. Random black hole particle swarm optimization and its application. In: 2008 International Conference on Neural Networks and Signal Processing. IEEE, pp. 359–365. https://doi.org/10.1109/icnnsp.2008.4590372.

Zhu, Y., Toon, O.B., Kinnison, D., et al., 2018. Stratospheric aerosols, polar stratospheric clouds, and polar ozone depletion after the mount calbuco eruption in 2015. J. Geophys. Res. Atmos. 123 (21), 331. https://doi.org/10.1029/2018JD028974, 12,308-312.